Radiation Physics and Chemistry 217 (2024) 111464

Contents lists available at ScienceDirect

Radiation Physics and Chemistry

journal homepage: www.elsevier.com/locate/radphyschem

Continuous and pulsed fast neutron beams at the CNA HiSPANoS facility

M.A. Millán-Callado [a,b], C. Guerrero [a,b,*], B. Fernández [b], J. Gómez-Camacho [a,b], M. Macías [a,b], J.M. Quesada [a]

[a] Dpt. Física Atómica, Molecular y Nuclear (FAMN), Facultad de Física. Universidad de Sevilla (US), 41012 Seville, Spain
[b] Centro Nacional de Aceleradores (CNA) (US-Junta de Andalucía-CSIC), 41092 Seville, Spain

ARTICLE INFO

Keywords:
Fast neutrons beam
Neutron detection
Time-of-flight
^{2}H(d,n)
Li(d,n)
Be(d,n)

ABSTRACT

The characteristics of the fast neutron beams produced in the HiSPANoS facility at Centro Nacional de Aceleradores (CNA) are presented. The neutrons are generated by deuteron beams from a 3 MV tandem accelerator in either continuous (5 μA) or pulsed (2 ns width, 500 kHz and 4% duty cycle) mode. In this work, the pulsed mode was used in a time-of-flight characterization of the produced neutron beams in terms of yield, flux, energy resolution, and background. The results were then validated through their comparison with previously published data.

Quasi-monoenergetic neutron beams between 2 and 6 MeV are produced by means of the $^{2}H(d,n)^{3}He$ reaction, featuring a neutron yield of 10^{6} n/sr/μC at the target, with an energy resolution of about 7% at 150 cm. Neutron beams with broad energy distributions are produced by deuteron irradiation of thick beryllium and lithium targets, resulting in maximum neutron energies of 10 and 20 MeV, respectively. In this case, the neutron yields are significantly higher, reaching 10^{10} n/sr/μC.

On the basis of these results, we consider that the HiSPANoS facility is now fully operational for the usage of fast neutrons by internal and external users of CNA.

1. Introduction

There is a growing interest in compact accelerator-based neutron sources (CANS) as a complement to major facilities, especially to support large-scale spallation neutron sources for basic research, technical developments, material analysis, and instrumentation (Anderson et al., 2016).

The relevant characteristics of neutron beams (energy, flux, and resolution) vary significantly. However, different applications have different requirements in terms of these characteristics. Regarding neutron energy, fast neutrons in the MeV range play a role in fission, fusion, material irradiation, detector characterization, radiation-to-electronic (R2E) studies, radioprotection, dosimetry, and others (Anderson et al., 2016). Regarding the time structure of the beams, pulsed beams are more scarce compared to the widespread continuous neutron beams, but their availability opens an additional broad range of research lines and applications.

To this end, neutron beams have to be produced out of pulsed ion beams, inheriting their temporal structure. This pulsed structure makes it possible to know the moment at which all the neutrons are emitted from the target, hence enabling the possibility of knowing their kinetic energy (which is crucial in many cases) from the corresponding time-of-flight (TOF). Furthermore, the time-of-flight technique allows for studying the characteristics of the neutron beams produced, which is essential not only for the corresponding time-of-flight experiments but also for planning and analyzing experiments with continuous neutron beams.

HiSPANoS is the first accelerator-driven neutron source in Spain and is capable of delivering both continuous and pulsed neutron beams. It is installed in the 3 MV Tandem accelerator system at Centro Nacional de Aceleradores (CNA, Seville, Spain) (Gómez-Camacho et al., 2021), a user facility included in the Spanish ICTS catalog (catalog of singular scientific and technological facilities).

Previous experiments have been carried out with continuous neutron beams, with either thermal (see Irazola et al., 2016 related to detector characterization), epithermal (see Praena et al., 2013, 2014 for activation cross-section measurements), or fast neutrons (see Malagón et al., 2017; Millán-Callado et al., 2019 for neutron irradiation and neutron imaging studies). In a first commissioning campaign of the pulsing system, Macías et al. (2020) completed the characterization of pulsed epithermal neutron beams produced via the Li(p,n) reaction near its threshold. In this context, the neutron field for the named reaction at 1950 keV, interesting for BNCT (Boron Neutron Capture Therapy) studies, was experimentally measured by the time-of-flight

* Corresponding author at: Dpt. Física Atómica, Molecular y Nuclear (FAMN), Facultad de Física. Universidad de Sevilla (US), 41012 Seville, Spain.
E-mail address: cguerrero4@us.es (C. Guerrero).

https://doi.org/10.1016/j.radphyschem.2023.111464
Received 21 June 2023; Received in revised form 20 September 2023; Accepted 8 December 2023
Available online 9 December 2023

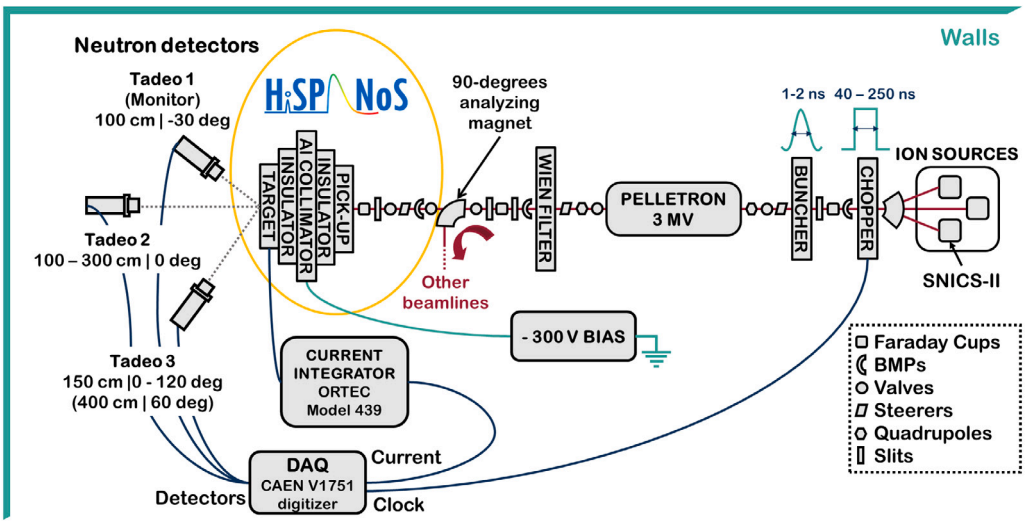

Fig. 1. Schematic view of the CNA Tandem accelerator, with the HiSPANoS neutron beamline at the far left end. The position of the neutron detectors and the electronic chain used during the commissioning is also indicated.

technique (Macías et al., 2021). In the work presented herein, the pulsing system is used to characterize, via time-of-flight, the wide variety of fast neutron beams that can be produced from deuteron-induced reactions on D, Li, and Be targets.

In the present work, the facility and the experimental set-up are described in Section 2. The results and their comparison to the expectations and data from literature for quasi-monoenergetic and broad energy neutron beams are presented in Sections 3 and 4, respectively. Finally, in Section 5 the results are summarized and the outlook of the research with fast neutron beams at HiSPANoS is presented.

2. Experimental setup

2.1. The 3 MV tandem accelerator

The accelerator system at CNA is a 3 MV 9SDH-2 Pelletron from National Electrostatics Corp. (NEC) capable of accelerating different ion species by making use of its three different ion sources. In particular, SNICS-II is a Cs sputtering source capable of producing both proton and deuteron beams with currents up to several tens of μA. The ion source is connected to an injection magnet that deflects the desired negative ions toward the entrance of the 3 MV tandem. In the HV terminal (in the middle of the acceleration tank), the ion charge changes into positive due to the electron stripping process that occurs in the N_2 gas, allowing the ions to be accelerated through the same high potential twice, reaching a maximum of 6 MeV, in the case of protons and deuterons, when terminal voltage is set to its nominal maximum of 3 MV. At the exit of the accelerator tank, a Wien filter and a 90-degree analyzing magnet select the required ion species. The beamline can either be deflected by the magnet to the 90-degree experimental lines or passed directly to a 0-degree beamline, where the HiSPANoS neutron beamline is located (Fig. 1).

2.1.1. HiSPANoS neutron beamline

The HiSPANoS neutron beamline is placed at 0 degrees from the accelerator tank. The line is equipped with elements for steering and monitoring the beam such as Faraday cups (FC) and beam profile monitors (BPM). A fast pickup, near the very end of the line, allows monitoring the passage of pulsed ion beams. To shape the ion beam, Ta slits and a 350 μm Al collimator with a variable opening are available (Fig. 1).

The targets for producing neutrons are held at the end of the beamline, at ~15 cm from the collimator, and electrically isolated from the rest of the beamline by a ceramic piece, thus allowing beam current monitoring. A voltage of −300 V is applied to the collimator in order to prevent the loss of secondary electrons emitted in the beam–target interaction, which would cause an overestimation of the beam current. The neutron production target is then connected to an ORTEC 439 Digital Current Integrator module, which produces a logic signal when a total charge of choice (usually set to 0.1 nC) is accumulated (Fig. 1).

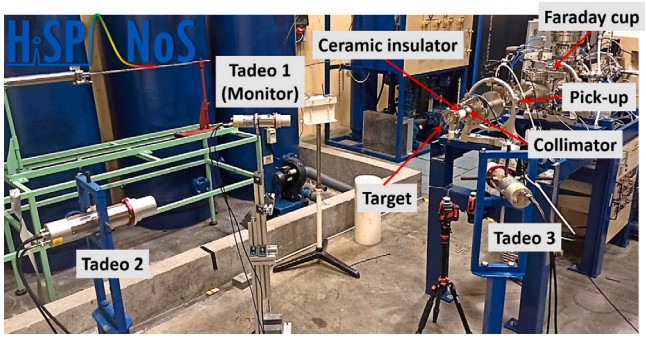

Fig. 2. Picture of the experimental set-up at HiSPANoS.

2.1.2. HiSPANoS pulsing system and experimental area

The accelerator, as described above, allows for continuous operation, producing continuous neutron beams. However, a recent upgrade allows for pulsed ion beams, hence opening the door to time-of-flight experiments.

This system, from NEC as well, is installed at the low energy stage of the accelerator, between the ion sources and the accelerator tank (Fig. 1, see details in Fernández et al.). It consists of a chopper and a buncher. The first element, the chopper, electrostatically deflects the ion beam out of the beamline with a frequency of choice (from 32.2 kHz to 2 MHz), producing ion pulses with a variable width from 40 to 250 ns. Then, the pulsed ion beam is compressed by the buncher, so that the initial pulse width of tens of ns is reduced to about 2 ns by the time it reaches the neutron production target, at the end of the beamline.

The HiSPANoS experimental area is in a corner of the accelerator hall (see Fig. 2). The target lies at 125 cm from the floor, with the two nearest walls at 4 m and the furthest ones at 16 m. This allows for a maximum flight path of up to 3 m in the forward direction. Longer

Table 1
Summary of the main reactions and targets used for fast neutron production at HiSPANoS.

Reaction	Q-value	E_{th}	Target		
	(MeV)	(MeV)	Material	Thickness	Diameter
$^{2}H(d,n)^{3}He$	3.27	0.0	D/Ti	546 μg/cm^2	30 mm
$^{9}Be(p,n)^{9}B$	−1.85	2.06	Be	500 μm	25 mm
$^{9}Be(d,n)^{10}B$	4.36	0.0			
$^{7}Li(p,n)^{7}Be$	−1.64	1.88	Li	500 μm	25 mm
$^{7}Li(d,n)^{8}Be$	15.03	0.0			

flight paths are available at other angles, for instance, measurements at up to 4 m have been performed at 60 degrees.

2.2. Neutron production reactions and targets

There are many nuclear reactions that result in the emission of neutrons. Considering the characteristics of the CNA's tandem accelerator, the most prolific neutron production corresponds to deuterons impacting on a thick target of either Li or Be. In addition, it is often needed to make irradiation or detector calibrations with quasi-monoenergetic neutron beams, which can be achieved with deuterons impinging on either ^{2}H or ^{3}H thin targets; however, the use of the latter at CNA is not currently feasible due to radioprotection issues.

The reactions employed for fast neutron production at HiSPANoS and the details of the corresponding targets are summarized in Table 1:

- The Be and Li targets are self-sustained foils in which the deuteron beam is fully stopped. They are attached to a 500 μm thick copper backing that closes the beamline, keeping it in vacuum. In the case of Li, a fresh disk is produced for each experiment due to the very rapid oxidation of metallic Li. The target holder, designed as described in (Praena et al., 2013) but made of Al instead of Cu, allows for either air or water cooling, the latter necessary for continuous irradiation of the Li target (which melts at 180 °C) with high current.
- The thin deuterium target is a commercially available design by SODERN (see Monning et al., 2002 for details) in which the deuterium is deposited in a titanium mesh of 30 mm in diameter attached to a 3 mm thick aluminum backing (D/Ti = 1.6). In this case, the beam traverses the thin D/Ti mesh and, depending on the beam energy, can produce spurious neutrons through reactions in both Ti and Al. To subtract those from the ^{2}H(d,n) neutrons, a blank "dummy" target has been used.

2.3. Detection system

Among the different types of fast neutron detectors available, liquid scintillators of 2"x2" by SCIONIX have been chosen for commissioning HiSPANoS. In comparison to fission chambers, these detectors are commercially available, feature larger efficiencies (thickness can be chosen on demand), are easy to operate, and allow implementing arrays covering simultaneously several angles and flight path distances. In this case, a total of three scintillators, one EJ-301 (Tadeo-1) and two EJ-309 (Tadeo-2 and Tadeo-3), all coupled to fast photomultipliers Model No. 9214 from ET Enterprises, have been used at different distances and angles from the neutron source.

The most relevant characteristics of a neutron detector used in neutron flux measurements are its neutron detection efficiency and its capacity to distinguish between neutron and γ-ray signals using Pulse Shape Discrimination (PSD).

2.3.1. Detector efficiency

The organic liquid scintillators used in this work are based on the detection of the signal produced mainly by the nuclear recoils when a neutron undergoes elastic scattering with the H or C nuclei of the material. As the signal amplitude depends on the energy of the incoming neutron, so does the detection efficiency, which is significantly affected by the detection threshold applied. Since the detectors have not been absolutely calibrated in a reference laboratory, the efficiency reported by Pino et al. Pino et al. (2014) for a similar detector with a reported accuracy of 7% has been assumed. The efficiency curves for 200 and 300 keVee thresholds are displayed in Fig. 3, together with the 9th degree polynomial functions used for the interpolation. In the analysis, the 200 keVee threshold was used for the monoenergetic neutron beams meanwhile the 300 keVee was applied to broad neutron beams.

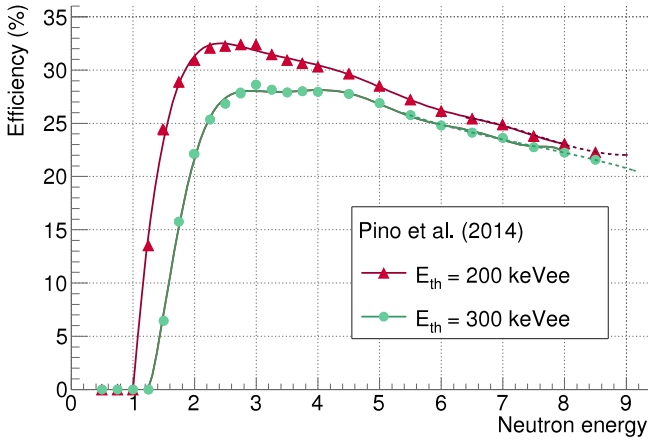

Fig. 3. Neutron efficiency for an EJ-309 2"x2" organic liquid detector from Pino et al. (2014) (with 7% accuracy), for the two energy thresholds used (200 and 300 keVee). The solid lines correspond to analytical fits with 9th degree polynomials.

2.3.2. Acquisition system and PSD

The detectors, the clock signal from the chopper, and the output of the current integrator are connected directly to the data acquisition system, without further electronic manipulation of the signal. This data acquisition system consists of a CAEN V1751 digitizer featuring 8 channels with a 10 bits resolution and a sampling rate of 1 GS/s. The CAEN software CoMPASS was used for configuring the different channels and for operating the DAQ in coincidence mode: the system analyzes the detector signals only when they are within a time coincidence window with respect to a reference channel, which is the chopper clock. For each signal, the DAQ returns a timestamp (corresponding to signals rising point above 25% of the maximum amplitude, i.e., a digital Constant Fraction Discriminator, CFD) and two values corresponding to the total (Q_{long}) or partial (Q_{short}) integrals of the signal. The start time of both integrals is well before the signal starts, then the partial integral (Q_{short}) stops slightly after the signal maximum, beyond which the γ-rays and neutron signal shapes become different. This is illustrated in Fig. 4, where the mentioned timestamp and the integration intervals are depicted. The relative difference between the two integrals, called PSD and given by Eq. (1), provides the means to differentiate between neutron and γ-ray signals by Pulse Shape Discrimination (PSD) (Brook, 1979), a capability of some scintillators related to the different linear

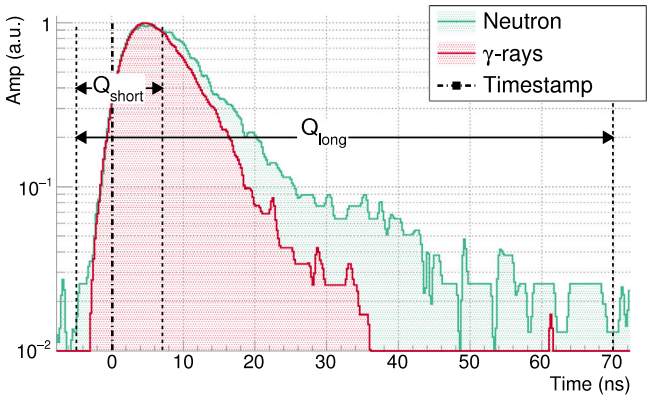

Fig. 4. Difference between neutron and γ-ray signals in the EJ-301 detector and definition of the signal parameters returned by the DAQ.

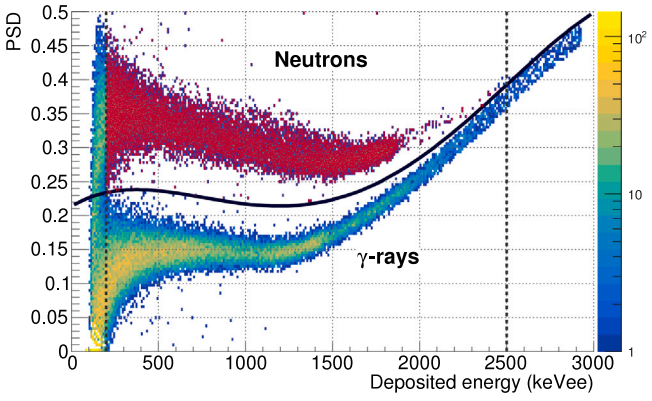

Fig. 5. Measured distribution of the PSD values obtained as a function of the signal energy measured for the ^{2}H(d,n) reaction with E_d = 1.5 MeV. The solid line represents the analytical function separating both particle types.

energy transfer (LET) of the nuclear recoils and electrons resulting from the neutron and γ-ray interactions, respectively.

$$PSD = \frac{Q_{long} - Q_{short}}{Q_{long}} \quad (1)$$

The distribution of the PSD values recorded from ^{2}H(d,n) reactions with a 1.5 MeV deuteron beam is represented in Fig. 5 as a function of the signal energy (in light equivalent keVee units, obtained from the calibration with ^{137}Cs, ^{22}Na and ^{60}Co sources). The data are clearly distributed along two branches, corresponding to neutrons (upper branch) and γ-ray (lower branch) signals. The separation between the two types of signals has been modeled by the 4th-degree polynomial, shown as a solid line. At low deposited energy, below ~200 keVee, the small size of the signals combined with the limited resolution of the digitizer and the non-negligible noise level prevents a very clear particle discrimination. The upward bending of the two distributions above 1300 keVee is related to the non-linear behavior of the voltage divider for larger signals, which affects more the partial (Q_{short}) than the total (Q_{long}) signal integrals. This limits the PSD capabilities to a maximum of 2500 keVee.

Overall, γ-ray and neutron signals are very well separated, as illustrated in Fig. 6. The PSD features a figure-of-merit (FoM) of 1.5, where FoM is defined by Eq. (2), as in Guerrero et al. (2008).

$$FoM = \frac{D_{n/\gamma}}{FWHM_n + FWHM_\gamma} \quad (2)$$

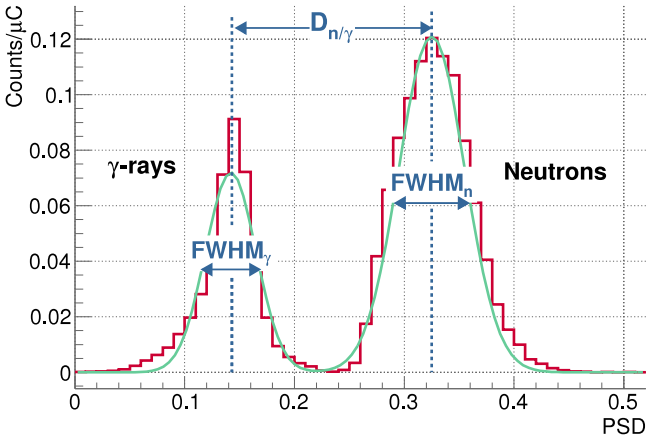

Fig. 6. PSD distribution for signals between 200 and 2500 keVee (projected from Fig. 5). The green line corresponds to a fit to two Gaussian distributions.

2.4. Beam, target, and detector configurations employed in the commissioning

The experiments carried out for the beam commissioning and the corresponding results are divided into two categories: ^{2}H(d,n) reactions yielding quasi-monoenergetic neutrons and thick target experiments yielding broad energy neutron beams.

The study of the energies and fluxes of quasi-monoenergetic neutrons that can be produced at HiSPANoS by means of the ^{2}H(d,n) reaction is interesting for future experiments requiring such beams, but also a very valuable tool for characterizing the energy resolution of the facility, as well as for studying the scattering neutron background inherent to a non-collimated facility such as HiSPANoS. Leaving the monitor detector (Tadeo-1) fixed at an angle of −30 degrees at a distance of 100 cm from the neutron source, the other two detectors (Tadeo-2 and Tadeo-3) were placed at a distance between 1 and 4 m and at angles between 0 and 120 degrees. The deuterium beam energy was changed between 750 and 3000 keV, producing quasi-monoenergetic beams between 2 and 6 MeV.

On the other hand, the reactions from deuterium beams impacting on the thick Li and Be targets, which produce neutron beams with a broad energy distribution, were only studied with Tadeo-2 placed in forward direction at a fixed flight path of 150 cm. This is considered a reference position that provides a reasonable energy resolution while keeping the wall effects negligible.

Additional measurements were performed for the background estimation. In particular, a shadow bar (10 cm of Pb followed by 50 cm of polyethylene, both with a diameter of 20 cm) was used to estimate the neutron scattering background in all configurations. In the case of the ^{2}H(d,n) reaction, the mentioned dummy target was used to study the neutrons produced in the Ti and Al present in the D/Ti target assembly.

3. Quasi-monoenergetic neutron beams

3.1. Time-of-flight (TOF) spectra

In each experiment, the output returned by the DAQ is a list of signals characterized by their time, Q_{short} and Q_{long}. The corresponding time-of-flight (TOF) histograms are produced by taking the chopper clock signal as a reference start time. The measured TOF is calibrated so that the γ-flash (a pronounced peak corresponding to the arrival of prompt γ-rays produced in the interaction of the pulsed ion beam with the target) is set to the time required by photons to travel the corresponding flight path, i.e. $t_{flash} = L_{TOF}/c$, where L_{TOF} is defined as the distance between the neutron production target and the center of the detector active volume (not the front face).

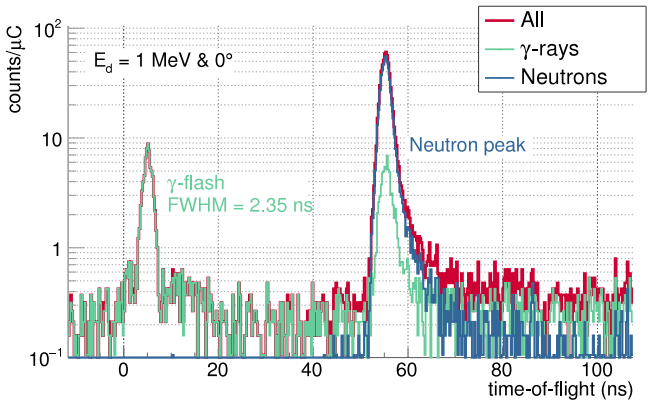

Fig. 7. TOF spectra for the ^{2}H(d,n) reaction at 1.0 MeV beam energy measured at 150 cm in the forward direction. The blue line corresponds to neutron signals (see Section 2.3.2).

Fig. 7 displays the result of the configuration of a 1.0 MeV deuteron beam hitting the D/Ti target, measured with Tadeo-2 at 150 cm distance in the forward direction. The two histograms correspond to all (red) and neutron only (blue) signals, illustrating the excellent PSD capabilities achieved. The γ-ray TOF distribution (green) features a constant level (environmental background) and the peak corresponding to the γ-flash. The γ-flash has a width of 2.35 ns corresponding to the time spread of the ion beam and, as mentioned above, serves as an accurate reference for the neutron production time. The neutron TOF distribution features a pronounced peak corresponding to neutrons of very well-defined energy, i.e. the quasi-monoenergetic neutrons resulting from the ^{2}H(d,n) reaction on the thin D target. The tail observed at longer TOF values, two orders of magnitude below the main neutron peak, is related to the deuterium diffusion into the backing (Nolte and Thomas, 2011).

3.2. Energy distributions

Due to the limited velocity of the neutrons ($v \ll c$), the TOF distributions can be transformed into neutron energy (E_n) distributions using the non-relativistic expression (3):

$$E_n(MeV) = \frac{1}{2} m_n v^2 = \left(\frac{72.293 \cdot L_{TOF}(m)}{TOF(ns)} \right)^2 \quad (3)$$

Applying this transformation to the TOF distribution from Fig. 7 (E_d = 1.0 MeV) results in the neutron energy distribution displayed in the top panel of Fig. 8. It features a very well-defined quasi-monoenergetic neutron beam centered at 4 MeV with a resolution of just 7%. The additional spectra shown in Fig. 8 (top) correspond to the measurements of the dummy target and the scattered background measured using a shadow bar. The bottom panel illustrates the situation for a higher energy deuteron beam of 3.0 MeV, which is enough to produce neutrons in the thin Ti substrate, the Al backing, the Al collimator, and the very thin C contamination layer built up on the surface of the target (Böttger et al., 1989). It must be considered that the ~11 MeV neutrons emitted in the Al collimator travel a longer distance (15 cm more) to reach the detector, therefore appearing at a lower reconstructed neutron energy of ~9 MeV. Another background contribution is generated by neutrons scattered across the room and then arriving at the detector, measured using the previously mentioned shadow bar. The subtraction of the dummy target and shadow bar contributions provides the aimed clean quasi-monoenergetic neutron beam. However, this is only feasible up to the maximum neutron energy of 6 MeV shown in the figure, since at higher beam energies, neutrons from other deuteron-induced reactions in the target represent the dominant contribution. In any case, even if another type of target was used, the quasi-monoenergetic neutron

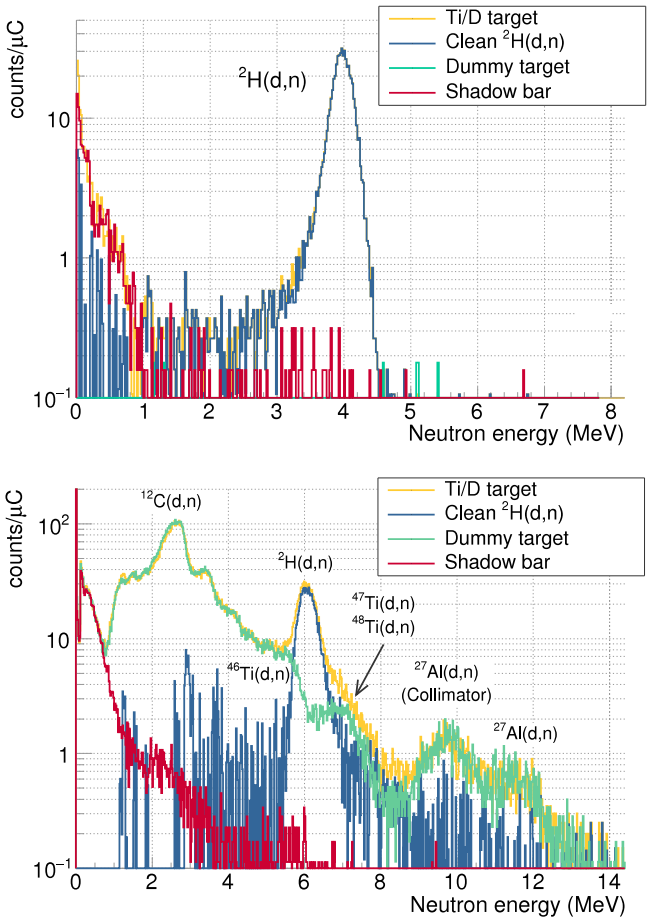

Fig. 8. Reconstructed neutron energy spectra measured with the D/Ti (with and without shadow bar) and dummy targets for E_d = 1.0 MeV (top) and E_d = 3.0 MeV (bottom). The aimed quasi-monoenergetic contribution from the ^{2}H(d,n) reaction is obtained after the background subtraction. The contribution of different reactions is labeled in the figure.

production though the ^{2}H(d,n) reactions cannot be pushed beyond ~7 MeV because the neutron emission from deuteron break-up becomes important at beam energies above ~3.7 MeV.

The energy of the neutrons emitted in the $^{2}H(d,n)$ reaction depends on both the ion beam energy and the angle of emission. In order to illustrate the quasi-monoenergetic neutron beams that can be produced at HiSPANoS, the angle of the detectors was changed between 0 and 120 degrees for a deuterium energy of 1.5 MeV, and the beam energy was changed between 0.75 and 3.0 MeV for three selected angles: 0, 30 and 120 degrees. The results are displayed in Fig. 9: as expected, the energy of the neutrons increases with the ion beam energy and decreases with the angle. This shows that HiSPANoS can provide neutron beams with well-defined energies from 2 to 6 MeV and that the wide range of angles available at the laboratory allows for multiple simultaneous neutron energy experiments without the need of changing the voltage of the accelerator.

The data from HiSPANoS in Fig. 9 was compared with the reference data of Liskien and Paulsen (1973), retrieved through the code NeuSDesc (Birgersson et al., 2009) developed at JRC-Geel. NeuSDesc results include the effect of a finite-size D/Ti target on the energy of the outgoing neutrons (dashed lines in the plot). The good agreement serves as validation of the beam energy value, detector positioning (distance and angle), TOF time calibration and neutron energy calculations presented herein.

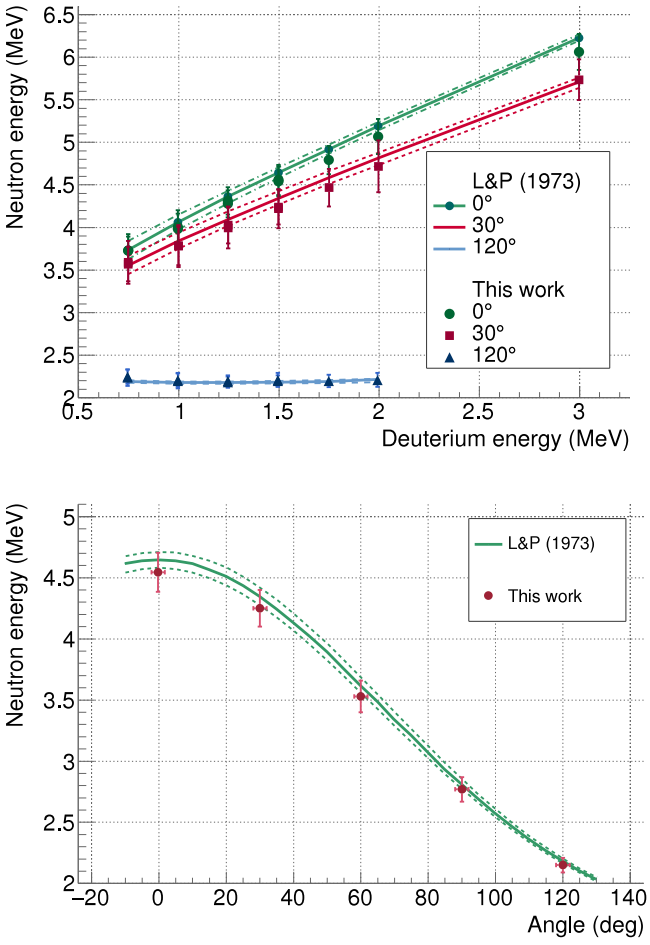

Fig. 9. Dependence of the neutron energy on the ion beam energy (top) and angle (bottom, E_d = 1.5 MeV). The lines correspond to the data of Liskien and Paulsen (1973), retrieved with NeuSDesc (Birgersson et al., 2009) (which also provides an estimation of the uncertainty). The uncertainties of the experimental data correspond to the measured resolution in Y and to the detector positioning (bottom) or the accelerator calibration (top) in X.

3.3. Energy resolution

Energy resolution is a key feature of a time-of-flight facility, and the availability of quasi-monoenergetic beams allows studying it accurately. Bearing in mind Eq. (3) and considering the propagation of uncertainties, the energy resolution can be calculated in Eq. (4):

$$R(E_n, L) = \frac{\Delta E_n}{E_n} = \sqrt{\left(\frac{2\Delta t}{t}\right)^2 + \left(\frac{2\Delta L}{L}\right)^2 + \left(\frac{\Delta E_n}{E_n}\right)^2_{target}}, \quad (4)$$

Hence, the resolution has contributions from the flight distance (L and ΔL), mainly the finite size of the detector; the time-of-flight (t and Δt), mainly the duration of the pulsed deuteron beam; and the energy spread of the neutrons due to the energy loss of the beam in the D/Ti target.

Experimentally, the neutron energy resolution of HiSPANoS has been determined from the energy and spread of the quasi-monoenergetic neutron peak at 3.6 MeV, produced by deuterons with 1.5 MeV at 60 degrees. This resolution has been studied as a function of the flight path up to 4 m.

The experimental and calculated energy resolutions are displayed in Fig. 10, showing a good agreement and illustrating how it improves with the flight path. The partial contributions to the resolution, also displayed in the figure, evidence that the dominant factor is the 2 ns width of the beam pulse.

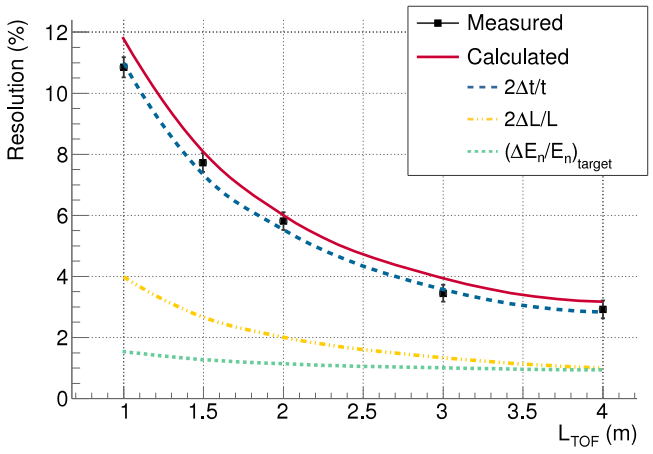

Fig. 10. Dependence of the neutron energy resolution on the flight path distance, measured at 60 degrees for 3.6 MeV neutrons. The expected behaviour is shown as a solid line, with the dashed lines corresponding to the partial contributions.

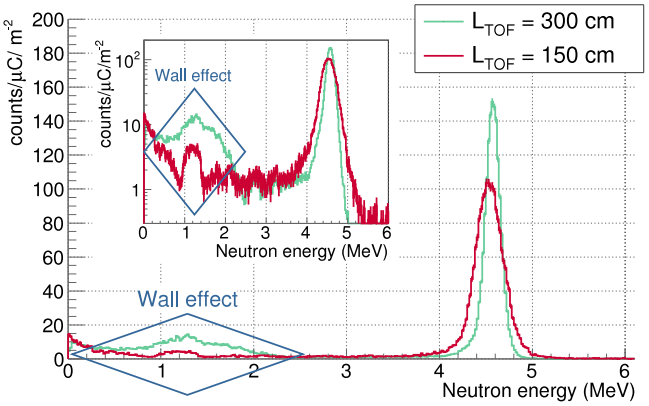

Fig. 11. Reconstructed neutron energy distribution for E_d = 1.5 MeV in forward direction, illustrating the wall effect (neutron scattering background) depending on the flight path. The spectra are normalized by L^{-2} in meters.

3.4. Neutron scattering: wall effects

Despite the neutron energy resolution being improved by the increasing flight path, the limited size of the experimental area is still an important factor to consider. Geometrically speaking, the dimensions of the tandem hall allow for a flight path of up to 3.5 m at 0 degrees and more than 4 m at 60 degrees. However, when the detector is close to the walls, structures start to appear in the measured spectra due to scattered neutrons, as shown in Fig. 11. The corresponding neutron energy distributions of two different flight path distances in forward direction for E_d = 1.5 MeV are represented in the figure. At 3 m, the detector is only 75 cm from the wall and thus a sizeable neutron scattered structure appears in the region between 1 and 2 MeV (in this example). A similar but much smaller structure appears when the detector is at only 1.5 m from the source, hence further from the wall.

3.5. Available beams

In order to determine the neutron flux emitted from the D/Ti source, the peaks observed in the clean neutron energy spectra (like those shown in Fig. 8) have been integrated and divided by the detection efficiency of the detector (see Fig. 3), the area of the detector's front surface and the time-integrated beam current. In this way, the neutron source flux is expressed in the usual units of n/cm^2/s at a given

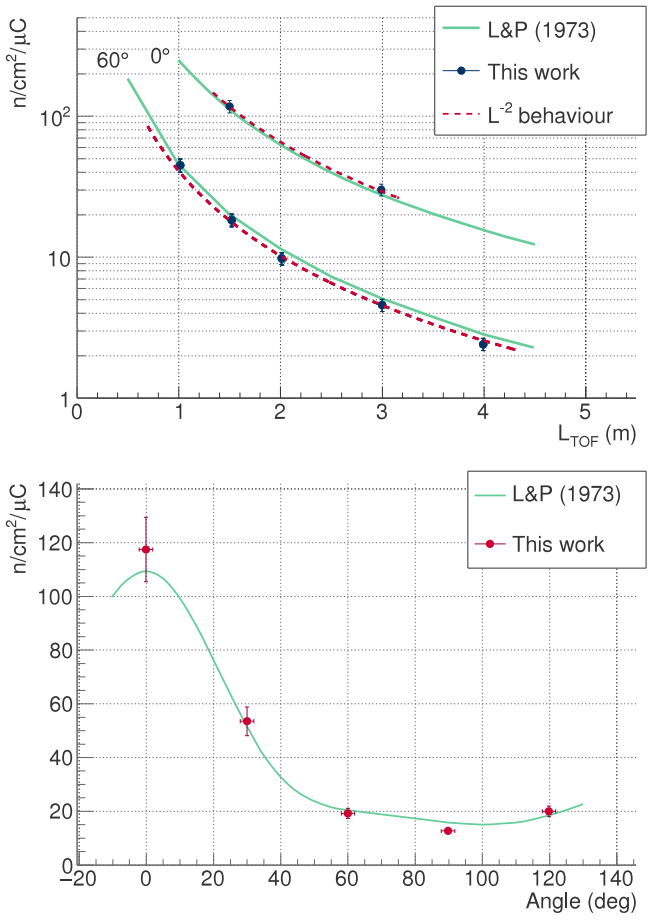

Fig. 12. Neutron flux measured at different distances (at 0 and 60 degrees) and angles (at 150 cm) with a deuteron beam of 1.5 MeV impacting on the D/Ti target. The solid lines correspond to the data of Liskien and Paulsen (1973) retrieved with NeuSDesc (Birgersson et al., 2009). The experimental data shows error bars on both axes.

distance. The neutron flux can then be easily transformed into n/sr/μC, as emitted at the source.

In the case of the ^{2}H(d,n) reactions, the neutron flux has been first studied for a fixed E_d = 1.5 MeV as a function of the flight path distance, in order to make sure that it follows the expected $1/{L_{TOF}}^2$ dependence. This is shown in Fig. 12 (top), where the values corresponding to Liskien and Paulsen (1973), retrieved again through NeuSDesc (Birgersson et al., 2009), are shown for validation. Since the experimental values follow the aforementioned dependence on the square of the distance, the subtraction of the background, which has been shown to increase with the distance from the neutron source, is thus validated. The figure also shows a variation up to a factor of six of the neutron flux with the angle (bottom). This is another proof of the correct background subtraction, since the neutrons scattered lose the angular information from the source and the experimental values are in very good agreement with the reference data.

Overall, Table 2 summarizes the configurations (beam energy and angle) available and the corresponding fluxes for quasi-monoenergetic neutron beams between 2 and 6 MeV. The beam energy of E_d = 1.5 MeV has been chosen for producing low-energy beams because, although neutron production is larger at higher energies, the background contribution from the target assembly is still negligible at this energy. In order to ease the beam time and counting rate estimation for potential users of the facility, the neutron flux in terms of n/cm^2/s for both continuous and pulsed beams is given, considering a reference distance of 150 cm, a 5 μA current and a 4% duty cycle. The corresponding neutron yield in n/sr/μC is also included in the table. The uncertainty in the flux is about 10%, considering the uncertainties in the detector efficiency (7% (Pino et al., 2014)), the finite thickness of the detectors at this distance (3%), and the reproducibility of the results from the neutron monitor (7%), which also includes a 3% accuracy in the beam current measurement. Other error sources have been deemed negligible.

4. Broad neutron beams

As opposed to the narrow energy beams produced in the interaction of the deuteron beam with the thin ^{2}H target, when the same beam impinges on a thick target it produces a broad energy neutron beam with much higher flux.

Given the energy range of the deuteron beam available at HiSPANoS, the reactions on thick Li and Be targets yield the highest neutron production. The neutron energies, according to the positive Q-values reported in Table 1, are up to 10 MeV for the Be target and exceeding 15 MeV for Li. Regarding the latter, a practical aspect to be considered is that while the melting point of Be is 986 ° C, that of Li is only 180 °C, thus requiring forced cooling when high beam currents are applied. At HiSPANoS, this is achieved by means of the water-cooled target holder mentioned in Section 2.2.

4.1. TOF/E_n spectra and scattering background

The time-of-flight spectra corresponding to the Li and Be targets when bombarded with the highest energy available (5.75 MeV) deuteron beams are displayed in Fig. 13.

In contrast to the case of the thin D/Ti target, the thick targets stop the ions completely, avoiding neutron production elsewhere and thus making a dummy target background subtraction unnecessary. Hence, only the background from scattered neutrons needs to be measured, with the help of the aforementioned shadow bar. This contribution to the time-of-flight and neutron energy distributions measured is illustrated in Fig. 13, in the form of light dashed lines. The neutron scattering background is especially relevant at long TOF (>110 ns), corresponding to low neutron energy (<1 MeV), as the detection efficiency for direct neutrons is smaller and eventually null, but scattered neutrons with high energies arriving to the detector at longer times can still be detected. However, the shadow bar method works well and allows an accurate subtraction of the neutron scattering background.

The time-of-flight and neutron energy distributions (displayed in Fig. 13) feature structures that are worth being discussed. Although all neutrons are produced by means of (d,n) reactions, when the deuteron brings enough energy to the system, the residual nucleus (^{8}Be in the case of Li and ^{10}B in the case of Be) can reach different excited states, which leaves less energy available to the emitted neutrons. Hence, there is a correspondence between the structures observed and the energy of these excited states, as illustrated in the bottom panel of Fig. 13. In this figure, the neutron energy (E_n) is subtracted from the total energy available (E_d+Q). The result demonstrates the correspondence between the observed structures and the well-known nuclear levels (labeled in the figure) in ^{8}Be and ^{10}B (IAEA - Nuclear Data Section, 2023).

4.2. Available beams

The background-subtracted neutron energy distributions corresponding to (d,n) reactions on Li and Be have been divided by the efficiency, the solid angle covered by the detector, and the integrated current in order to be transformed into units of neutron flux (n/sr/MeV/μC).

The result is displayed in Fig. 14, with the uncertainty in the neutron energy calculated from Eq. (4) and the 10% uncertainty in the neutron flux discussed in Section 3.5. The figure also includes a line

Table 2
Summary of the quasi-monoenergetic neutron beams available at HiSPANoS (intermediate energy configurations are also available). The neutron yield is given in n/sr/μC. The neutron flux at a distance of 150 cm for both continuous and pulsed neutron beams, considering a 5 μA current and a 4% duty cycle, is given in n/cm^2/s.

E_d (MeV)	θ (deg)	E_n (MeV)	ΔE/E	*Yield* ($n/sr/\mu C$)	Flux (n/cm^2/s)	
					Continuous	*Pulsed*
1.5	120	2.2	5%	$4.5(4)\cdot10^5$	100(10)	4.0(4)
1.5	90	2.8	7%	$2.7(3)\cdot10^5$	60(6)	2.4(2)
1.5	60	3.5	8%	$4.1(4)\cdot10^5$	90(9)	3.6(4)
1.5	30	4.2	7%	$1.2(1)\cdot10^6$	270(30)	11(1)
1.5	0	4.5	7%	$2.6(2)\cdot10^6$	590(20)	23(2)
2.0	0	5.1	8%	$3.1(3)\cdot10^6$	680(30)	27(3)
3.0	0	6.1	7%	$3.7(4)\cdot10^6$	830(30)	33(3)

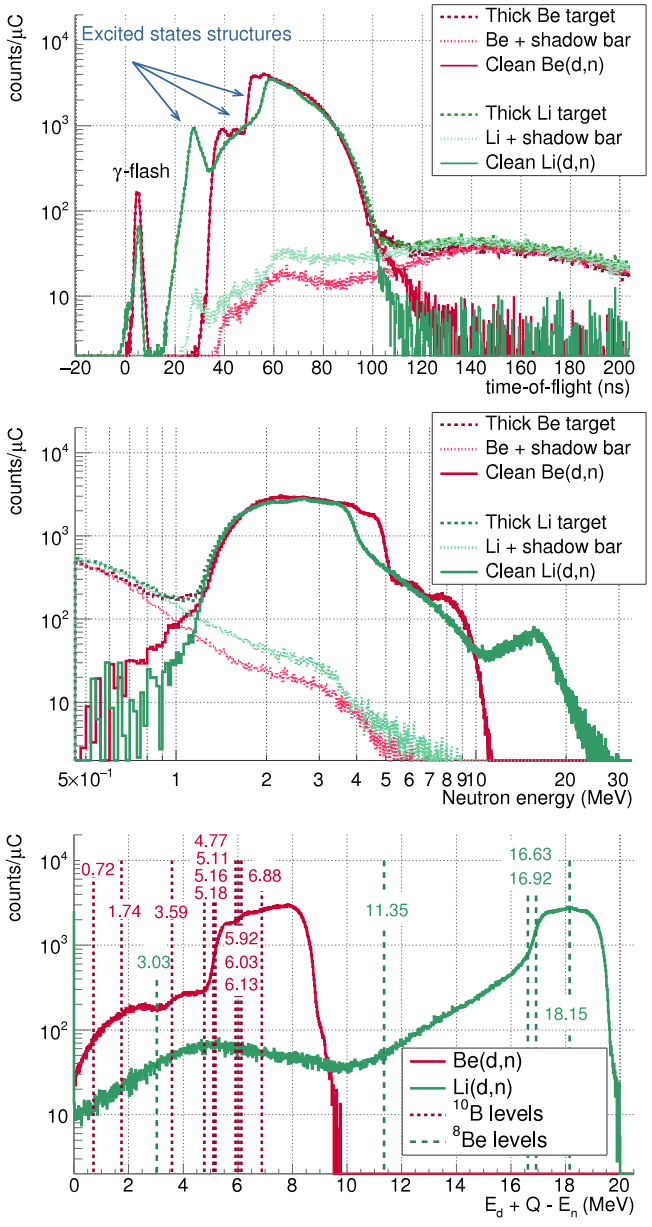

Fig. 13. Time-of-flight (top), neutron energy (middle) and E_d+Q-E_n (bottom) spectra for E_d = 5.75 MeV on the thick Li and Be targets measured forward at 150 cm. See text for details.

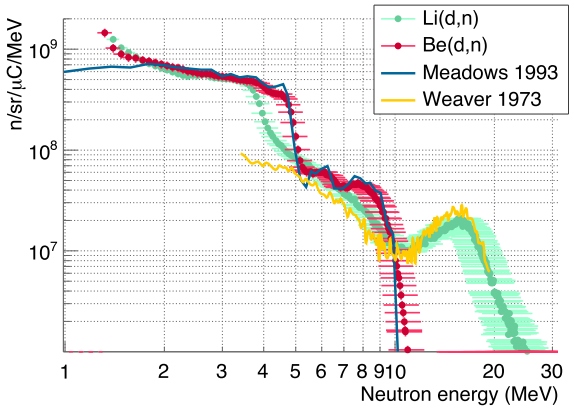

Fig. 14. Neutron yields at E_d = 5.75 MeV and a flight path of 150 cm in the forward direction for the Li and Be thick targets. The blue line corresponds to the data from Meadows (Meadows, 1993) for 5.8 MeV deuteron beams at 0° and the yellow line corresponds to the data from Weaver (Weaver et al., 1973) at 5.0 MeV and 3.5° (retrieved from EXFOR (Otuka et al., 2014) F0218.015).

corresponding to the data reported by Meadows (Meadows, 1993) for a 5.8 MeV deuteron beam impinging on a thick Be target, referred to the forward direction; and also the data from Weaver (Weaver et al., 1973) with a deuteron beam of 5.0 MeV impinging on a thick Li target and measured at 3.5°. There is indeed an excellent agreement between the HiSPANoS and Meadows data in terms of both energy distribution and neutron flux and, in the case of Weaver, the neutron flux from HiSPANoS is slightly higher in the energy region from 3 to 10 MeV, which is expected due to the difference in the deuteron energy and the measuring angle. The comparison at low energy (<2 MeV) between this work and Meadows evidences the limitations when measuring neutrons below 1–2 MeV with liquid scintillators, as in this work, compared to measurements with fission chambers, as in Meadows. The drop in the efficiency (see Fig. 3) and the corresponding higher uncertainty is responsible for the discrepancies near the energy threshold. Then, the better energy resolution of Meadows and Weaver, related to the longer flight path used (3.75 and 11 m respectively against 1.5 m), is only and barely visible at the fall-off around 10 MeV in the case of Be, and 15 MeV in the case of Li. The energy resolution is also responsible for showing neutron energies beyond 20 MeV, which is the physical limit according to the Q-value and the beam energy.

The broad energy neutron beams available at HiSPANoS are summarized in Table 3. Integral neutron production refers to neutrons above 1.3 MeV, which is the lower energy limit in the detection efficiency of the liquid scintillators used for neutron detection. As in the case of the quasi-monoenergetic neutron beams, the neutron fluxes for the continuous and pulsed beam configuration at a distance of 150 cm are given in units of n/cm^2/s, and the neutron yield at the target is given in n/sr/μC.

Table 3
Summary of the broad energy neutron beams available at HiSPANoS (intermediate energy configurations are also available). The neutron yield is given in n/sr/μC, and the neutron flux at a distance of 150 cm for both continuous and pulsed neutron beams is given in n/cm^2/s.

Reaction	E_d	Max. E_n	Yield	Flux (n/cm^2/s)	
	(MeV)	(MeV)	$(n/sr/\mu C)$	*Continuous*	*Pulsed*
Li(d,n)	5.75	20.6	$2.2(2)\cdot10^{10}$	$5.0(5)\cdot10^{6}$	$2.0(2)\cdot10^{5}$
Be(d,n)	5.75	10.1	$2.5(3)\cdot10^{10}$	$5.4(5)\cdot10^{6}$	$2.2(2)\cdot10^{5}$

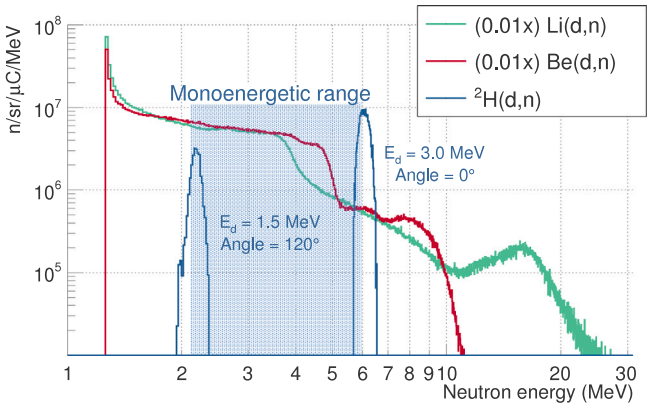

Fig. 15. Neutron yields at 150 cm for the main fast neutron beams available at HiSPANoS. Intermediate quasi-monoenergetic neutron beams and error bars have been omitted for clarity.

5. Summary and outlook

Since 2013, the HiSPANoS facility at CNA has operated in continuous mode as the first accelerator-based neutron source in Spain. In 2018, the setup was upgraded with a pulsing system producing ~2 ns pulses that enable new fields of research and applications using time-of-flight techniques. While the capability of HiSPANoS to produce pulsed epithermal neutron beams has already been assessed (Macías et al., 2020, 2021), this work is devoted to the commissioning of the fast neutron beams.

Continuous and pulsed fast neutron beams are produced at HiSPANoS by making a deuteron beam of up to 6 MeV and ~5 μA interact with the different targets available. While a thin deuterated titanium (D/Ti) target produces quasi-monoenergetic beams between 2 and 6 MeV, the use of thick Be and Li targets produces neutron beams with a broad energy distribution up to 10 MeV and over 15 MeV, respectively.

In this work, the neutron energy, resolution, background, and neutron flux of the different beams available at HiSPANoS (for different targets, beam energies, angles, and distances) have been characterized and shown to be in agreement with the expectations from existing reference data. As a summary, Fig. 15 shows some of the neutron beams available in units of n/sr/μC/MeV in the forward direction (except for the lowest energy quasi-monoenergetic neutron beam of 2.2 MeV, which corresponds to 120 degrees). The corresponding neutron yields at the target are in the order of 10^6 and 10^{10} n/sr/μC for quasi-monoenergetic and broad energy neutron beams, respectively (see details in Tables 2 and 3). The reported 10% accuracy in the neutron fluxes described in this work is dominated by a 7% contribution from detector efficiency (which could be reduced by using an absolutely calibrated neutron detector) and another 7% from the reproducibility of the results. There is ongoing work at CNA aimed to reduce the latter.

CRediT authorship contribution statement

M.A. Millán-Callado: Methodology, Software, Validation, Formal analysis, Investigation, Writing – original draft. **C. Guerrero:** Conceptualization, Methodology, Formal analysis, Investigation, Resources, Writing – review & editing, Supervision, Project administration. **B. Fernández:** Conceptualization, Methodology, Formal analysis, Investigation, Writing – review & editing, Supervision. **J. Gómez-Camacho:** Resources, Supervision, Funding acquisition. **M. Macías:** Investigation. **J.M. Quesada:** Resources, Supervision, Funding acquisition.

Declaration of competing interest

The authors declare the following financial interests/personal relationships which may be considered as potential competing interests: Begona Fernandez reports financial support was provided by Government of Andalusia. Jose Manuel Quesada reports financial support was provided by Spain Ministry of Science and Innovation. Carlos Guerrero reports financial support was provided by Spain Ministry of Science and Innovation. Jose Manuel Quesada reports financial support was provided by European Commission.

Data availability

Data will be made available on request and published in the IAEA EXFOR compilation of experimental nuclear reaction data (Otuka et al., 2014).

Acknowledgments

The authors thank the operators of the CNA Tandem accelerator (J.A. Labrador, D. Pascual-Álvarez, A. J. Romero and M. A. Seller) for their dedication and help in the commissioning of the pulsed neutron beams.

This work has received funding from the Euratom research and training program 2014–2018 under the grant agreement No 847594 (H2020-Euratom-ARIEL), the Marie Curie actions of the 7th Framework Program under the grant agreement No 334315 (FP7-PEOPLE-NeutANdalus), the Spanish national projects FPA2016-77689-C2-1-R, RTI2018-098117-B-C21, and PID2021-123879OB-C21; and the FEDER Andalucía funds under the project US-1261006.

References

Anderson, I.S., et al., 2016. Research opportunities with compact accelerator-driven neutron sources. Phys. Rep. 654, 1–58. http://dx.doi.org/10.1016/j.physrep.2016.07.007.

Birgersson, E., Loevestam, G., et al., 2009. NeuSDesc-neutron source description software manual. (ISSN: 1018-5593) EUR 23794 EN.

Böttger, R., et al., 1989. Problems associated with the production of monoenergetic neutrons. Nucl. Instrum. Methods Phys. Res. A 282, 358–367. http://dx.doi.org/10.1016/0168-9002(89)90167-8.

Brook, F.D., 1979. Development of organic scintillators. Nucl. Instrum. Methods 162, 477–505. http://dx.doi.org/10.1016/0029-554X(79)90729-8.

Fernández, B., et al., in press.

Gómez-Camacho, J., et al., 2021. Research facilities and highlights at the Centro Nacional de Aceleradores (CNA). Eur. Phys. J. Plus 3, 136. http://dx.doi.org/10.1140/epjp/s13360-021-01253-x.

Guerrero, C., et al., 2008. Analysis of the BC501A neutron detector signals using the true pulse shape. Nucl. Instrum. Methods Phys. Res. A 597, 212–218. http://dx.doi.org/10.1016/j.nima.2008.09.017.

IAEA - Nuclear Data Section, 2023. Live chart of nuclides. https://www-nds.iaea.org/relnsd/vcharthtml/VChartHTML.html. (Accessed 21 January 2023).

Irazola, L., et al., 2016. Using a Tandem Pelletron accelerator to produce a thermal neutron beam for detector testing purposes. Appl. Radiat. Isot. 107, 330–334. http://dx.doi.org/10.1016/j.apradiso.2015.11.020.

Liskien, H., Paulsen, A., 1973. Neutron production cross sections and energies for the reactions T(p, n)3He, D(d, n)3He, and T(d, n)4He. At. Data Nucl. Data Tables 11, 569–619. http://dx.doi.org/10.1016/S0092-640X(73)80081-6.

Macías, M., et al., 2020. The first neutron time-of-flight line in Spain: Commissioning and new data for the definition of a neutron standard field. Radiat. Phys. Chem. 168, 108538. http://dx.doi.org/10.1016/j.radphyschem.2019.108538.

Macías, M., et al., 2021. The first neutron time-of-flight line in Spain: Commissioning and new data for the definition of a neutron standard field. Radiat. Phys. Chem. 185, 109474. http://dx.doi.org/10.1016/j.radphyschem.2021.109474.

Malagón, D., et al., 2017. Soft error rate comparison of 6T and 8T SRAM ICs using mono-energetic proton and neutron irradiation sources. Microelectron. Reliab. 78, 38–45. http://dx.doi.org/10.1016/j.microrel.2017.07.093.

Meadows, J.W., 1993. The ^{9}Be(d, n) thick-target neutron spectra for deuteron energies between 2.6 and 7.0 MeV. Nucl. Instrum. Methods Phys. Res. A 324, 239–246. http://dx.doi.org/10.1016/0168-9002(93)90983-O.

Millán-Callado, M.A., et al., 2019. Neutron radiography at CNA. In: Basic Concepts in Nuclear Physics: Theory, Experiments and Applications. In: Springer Proceedings in Physics, vol. 225, pp. 153–154. http://dx.doi.org/10.1007/978-3-030-22204-8.

Monning, C., et al., 2002. Optimisation of the manufacturing process of tritide and deuteride targets used for neutron production. Nucl. Instrum. Methods Phys. Res. A 480, 214–222. http://dx.doi.org/10.1016/S0168-9002(01)02094-0.

Nolte, R., Thomas, D.J., 2011. Monoenergetic fast neutron reference fields: I. Neutron production. Metrologia 48, S263. http://dx.doi.org/10.1088/0026-1394/48/6/S04.

Otuka, N., et al., 2014. Towards a more complete and accurate experimental nuclear reaction data library (exfor): international collaboration between nuclear reaction data centres (nrdc). Nucl. Data Sheets 120, 272–276. http://dx.doi.org/10.1016/j.nds.2014.07.065.

Pino, F., et al., 2014. The light output and the detection efficiency of the liquid scintillator EJ-309. Appl. Radiat. Isot. 89, 79–84. http://dx.doi.org/10.1016/j.apradiso.2014.02.016.

Praena, J., et al., 2013. Measurement of the MACS of^{181}Ta(n, γ) at kT=30 keV as a test of a method for Maxwellian neutron spectra generation. Nucl. Instrum. Methods Phys. Res. A 727, 1–6. http://dx.doi.org/10.1016/j.nima.2013.05.151.

Praena, J., et al., 2014. Nucl. Data Sheets 120, 205–207. http://dx.doi.org/10.1016/j.nds.2014.07.047.

Weaver, K.A., et al., 1973. Neutron spectra from deuteron bombardment of D, Li, Be, and C. Nucl. Sci. Eng. 52, 35–45. http://dx.doi.org/10.13182/NSE73-A23287.